**Rapid growth of organic aerosol nanoparticles over a wide tropospheric temperature range**

# Rapid growth of organic aerosol nanoparticles over a wide tropospheric temperature range

**Dominik Stolzenburg[a], Lukas Fischer[b], Martin Heinritzi[c], Meredith Schervish[d], Mario Simon[c], Lubna Dada[e], Lauri R. Ahonen[e], Antonio Amorim[f], Andrea Baccarini[g], Paulus S. Bauer[a], Bernhard Baumgartner[a], Anton Bergen[c], Federico Bianchi[e], Martin Breitenlechner[b,h], Sophia Brilke[a], Stephany Buenrostro Mazon[e], Dexian Chen[d], António Dias[f,i], Danielle C. Draper[j], Jonathan Duplissy[e], Imad El Haddad[g], Henning Finkenzeller[k], Carla Frege[g], Claudia Fuchs[g], Olga Garmash[e], Hamish Gordon[l,i], Xucheng He[e], Johanna Helm[c], Victoria Hofbauer[d], Christopher R. Hoyle[m], Changhyuk Kim[n,o], Jasper Kirkby[c,i], Jenni Kontkanen[e], Andreas Kürten[c], Katrianne Lehtipalo[e], Markus Leiminger[b], Huajun Mai[n], Serge Mathot[i], Bernhard Mentler[b], Ugo Molteni[g], Wei Nie[p], Tuomo Nieminen[q], Andrea Ojdanic[a], Antti Onnela[i], Monica Passananti[e], Tuukka Petäjä[e], Lauriane L. J. Quéléver[e], Matti P. Rissanen[e], Nina Sarnela[e], Simon Schallhart[e,r], James N. Smith[j], Christian Tauber[a], António Tomé[s], Alexander L. Vogel[c,i], Andrea C. Wagner[c], Robert Wagner[e], Mingyi Wang[d], Lena Weitz[c], Daniela Wimmer[e], Mao Xiao[g], Chao Yan[e], Penglin Ye[d,t], Qiaozhi Zha[e], Urs Baltensperger[g], Joachim Curtius[c], Josef Dommen[g], Richard C. Flagan[n], Markku Kulmala[e], Douglas R. Worsnop[e,t], Armin Hansel[b], Neil M. Donahue[d], and Paul M. Winkler[a,1]**

[a]Faculty of Physics, University of Vienna, 1090 Vienna, Austria; [b]Institute for Ion Physics and Applied Physics, University of Innsbruck, 6020 Innsbruck, Austria; [c]Institute for Atmospheric and Environmental Sciences, Goethe University Frankfurt, 60438 Frankfurt am Main, Germany; [d]Center for Atmospheric Particle Studies, Carnegie Mellon University, Pittsburgh, PA 15213, USA; [e]Institute for Atmospheric and Earth System Research/Physics, Faculty of Science, University of Helsinki, 00014 Helsinki, Finland; [f]CENTRA and FCUL, University of Lisbon, 1749-016 Lisbon, Portugal; [g]Laboratory of Atmospheric Chemistry, Paul Scherrer Institute, 5232 Villigen, Switzerland; [h]John A. Paulson School of Engineering and Applied Sciences and Department of Chemistry and Chemical Biology, Harvard University, Cambridge, MA 02138, USA; [i]CERN, 1211 Geneva, Switzerland; [j]Department of Chemistry, University of California, Irvine, CA 92617, USA; [k]University of Colorado Boulder, Boulder, CO 80309, USA; [l]School of Earth and Environment, University of Leeds, LS2 9JT Leeds, UK; [m]Institute for Atmospheric and Climate Science, ETH Zurich, 8092 Zurich, Switzerland; [n]California Institute of Technology, Pasadena, CA 91125, USA; [o]Department of Environmental Engineering, Pusan National University, 46241 Busan, Republic of Korea; [p]Joint International Research Laboratory of Atmospheric and Earth System Sciences, Nanjing University, 210023 Nanjing, China; [q]Department of Applied Physics, University of Eastern Finland, 70211 Kuopio, Finland; [r]Finnish Meteorological Institute, 00101 Helsinki, Finland; [s]IDL, University of Beira Interior, 6200 Covilhã, Portugal; [t]Aerodyne Research Inc., Billerica, MA 01821, USA

This manuscript was compiled on May 2, 2018

**Nucleation and growth of aerosol particles from atmospheric vapors constitutes a major source of global cloud condensation nuclei (CCN). The fraction of newly-formed particles that reaches CCN sizes is highly sensitive to particle growth rates, especially for particle sizes below 10 nm where coagulation losses to larger aerosol particles are greatest. Recent results show that some oxidation products from biogenic volatile organic compounds are major contributors to particle formation and initial growth. However, whether oxidized organics contribute to particle growth over the broad span of tropospheric temperatures remains an open question, and quantitative mass balance for organic growth has yet to be demonstrated at any temperature. Here, in experiments performed under atmospheric conditions in the CERN CLOUD chamber, we show that rapid growth of organic particles occurs over the range from -25°C to +25°C. The lower extent of auto-oxidation at reduced temperatures is compensated by the decreased volatility of all oxidised states. We could reproduce the measured growth rates using an aerosol growth model based entirely on the experimentally-measured gas-phase spectra of oxidized organic molecules using two complementary mass spectrometers. We show that the growth rates are sensitive to particle curvature and display a clear acceleration as the particles increase in size, corresponding to a Kelvin diameter of 4.8±0.8 nm at 300 K, explaining widespread atmospheric observations that particle growth rates increase in the single-digit-nm size range. Our results demonstrate that organic vapours can contribute to particle growth over a wide range of tropospheric temperatures from molecular cluster sizes onward.**

aerosol particles | nanoparticle growth | atmospheric aerosol formation | CERN CLOUD experiment

The global budget of cloud condensation nuclei (CCN) has a significant impact on the Earth's radiative balance, as it affects the albedo and the lifetime of clouds. New particle formation by gas-to-particle conversion is the largest source of CCN (1). Especially the early steps of particle growth between 1-10 nm determine the survival chance of freshly formed particles and therefore their climatic relevance (2, 3). The major vapours driving particle growth are sulfuric acid and, maybe more importantly, low volatility organics resulting from the oxidation of volatile organic compounds (VOCs) (4). Monoterpenes are an important class of atmospheric VOCs with copious emissions from vegetation (5). They are quickly oxidized in the atmosphere and through a subsequent auto-oxidation process

## Significance Statement

Aerosol particles can form and grow by gas-to-particle conversion and eventually act as seeds for cloud droplets, impacting the global climate. Volatile organic compounds emitted from plants are oxidized in the atmosphere and the resulting products drive particle growth. We measure particle growth by oxidized biogenic vapors with a well-controlled laboratory setup over a wide range of tropospheric temperatures. While higher temperatures lead to increased reaction rates and concentrations of highly oxidized molecules, lower temperatures allow additional, but less oxidized, species to condense. We measure rapid growth over the full temperature range of our study, indicating that organics play an important role in aerosol growth throughout the troposphere. Our finding will help to sharpen the predictions of global aerosol models.

D.S., L.F., M.H., M.Shervish, M.Simon, L.D., H.G., A.H., J.Kirkby, M.K., K.L., M.P.R., P.M.W. were involved in the scientific discussion and interpretation of the results; D.S., L.F., M.H., M.Shervish, M.Simon, A.C.W., R.W., L.W., L.D. analysed the main data sets; D.S., L.F., J.Kirkby, N.M.D., P.M.W. wrote the manuscript; all other authors contributed to the design of the facility, preparation of the instruments or data collection and analysis, and commented on the manuscript.

The authors declare no conflict of interest.

[1]Paul Winkler. E-mail: paul.winkler@univie.ac.at

rapidly form highly oxygenated molecules (HOMs), which constitute a large source of low-volatility species in the atmosphere (6). Recent studies have shown that HOMs from the ozonolysis of the predominant monoterpene $\alpha$-pinene are able to form (7) and efficiently grow particles from cluster sizes onward (8). Model simulations suggest that they are major contributors to particle formation on a global scale (9). Moreover, the impact of HOMs on initial particle growth might explain the observations of accelerating growth rates between 1-10 nm during particle formation events (10) by a multi-component Kelvin effect (8, 11), also known as nano-Köhler theory (12). This is because HOMs span a wide range of volatilities (13) and, with increasing particle size, more and more low-volatile species can contribute to the growth process.

In contrast to sulfuric acid in combination with ammonia or amines, where growth proceeds close to the kinetic limit (14), the characteristics of growth driven by organics are governed by the resulting volatilities of the wide variety of oxidation products. Therefore, temperature likely plays a decisive role as the saturation concentration has a steep exponential temperature-dependence as described by the Clausius-Clapeyron relation. Additionally, a recent study has shown that temperature crucially influences the chemical composition of the initially formed molecular clusters in $\alpha$-pinene ozonolysis (15). Therefore, the contribution of biogenic organics to new particle formation might be strongly sensitive to temperature. This, in turn, may significantly influence the importance of new particle formation at high altitudes (16) and in outflow regions of deep-convective clouds, e.g. over the Amazon Basin (17–19).

Here we investigate in the CLOUD chamber (20) the effect of temperature on the production of oxygenated molecules and subsequent particle growth from dark $\alpha$-pinene ozonolysis at three different temperatures (-25°C, +5°C, and +25°C) for various precursor concentrations. The resulting volatility distributions are inferred by combining two types of chemical-ionisation high resolution mass spectrometers (21, 22) using different ionization techniques in order to obtain a detailed representation of the gaseous oxidation products. Together with the precision measurement of particle growth rates (23) this allows identification of the underlying processes and their temperature dependence responsible for initial growth in biogenic ozonolysis systems (See Methods for details about the experimental setup, measurement procedures and used instrumentation).

## Results

**Observed gas phase mass spectrum.** Fig.1 shows mass defect plots from the Nitrate-CI-APi-ToF (Nitrate-CI) (21) and the PTR3-ToF (PTR3) (22) during three representative experiments at three different temperatures. For all three cases, we averaged the observed gas-phase concentrations $C^v$ over a period where comparable particle growth rates are measured with a DMA-train (23) and the $\alpha$-pinene ozonolysis rate is similar with $[\mathrm{k}(T) \cdot \mathrm{ap} \cdot \mathrm{O_3}] \sim 1.4 - 2.0 \cdot 10^6 \mathrm{cm^{-3}s^{-1}}$.

The mass defect plots for all temperatures show the typical pattern of HOMs (8). Two bands can be identified, one representing monomers ($n_C$=6-10, 100-400 Th) and one representing dimers ($n_C$=16-20, 400-600 Th); molecules with increasing oxidation state are found towards the lower right of the panels. Apparently, the PTR3 introduces more than 200 previously

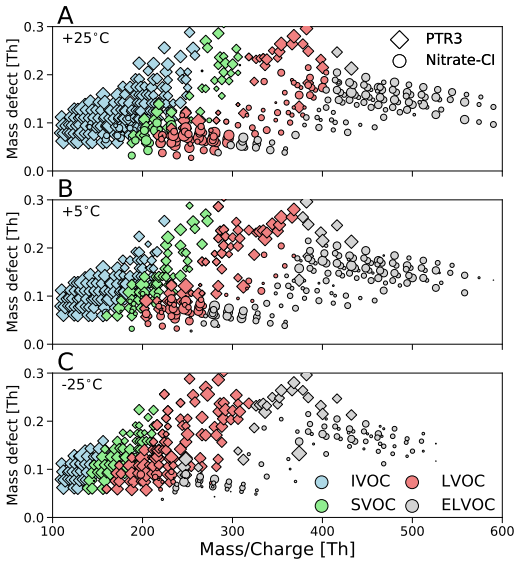


**Fig. 1.** Mass defect of all measured neutral oxidized organic compounds versus the nominal mass to charge ratio of three representative experiments, at +25°C (A), at +5°C (B) and at -25°C (C), all with a similar $\alpha$-pinene ozonolysis reaction rate. Diamonds represent molecular ions measured by the PTR3 and circles compounds measured by the Nitrate-CI, both taking the different reagent ions into account. The size of the symbols is proportional to the logarithm of the measured concentration and the color is related to the volatility class as defined in Fig. S3.

undetected molecular ion signals, not only HOMs, which are usually specified by their high O:C ratio (>0.7 for monomers), but mostly compounds towards lower oxidation states.

As temperature decreases, the intensity of the majority of the peaks drops, especially for compounds with a high oxidation state and with a high detection efficiency in the Nitrate-CI. This is similar to the observations by (15), where a significant decrease in O:C ratio of the nucleating charged clusters was observed during the same set of experiments.

In Fig.1, the symbol color for peaks with an identified composition corresponds to a broad temperature-dependent classification of their volatility, based on the carbon and oxygen numbers of the individual compounds (see Supporting Information for detailed information on the volatility classification and its temperature dependence). We place them in four general groups, according to their saturation mass concentration $C^*$: extremely low volatility compounds (ELVOC, $\log_{10} C^* \leq$-4.5), low volatility compounds (LVOC, $\log_{10} C^*$=(-4.5,-0.5]), semi-volatile compounds (SVOC, $\log_{10} C^*$=(-0.5,2.5]) and intermediate volatility compounds (IVOC, $\log_{10} C^* >$2.5) (13). Compounds in the ELVOC and LVOC ranges have been shown to contribute to nanoparticle growth (8). Comparing this classification for the three different temperatures clearly indicates the importance of the compounds observed by the PTR3. At -25°C, large quantities of LVOC compounds can be observed by the usage of this additional ionization technique.

**Observed volatility distribution within a volatility basis set (VBS).** As volatilities of organic compounds observed in the atmosphere vary by more than 10 orders of magnitude, it is convenient to simplify considerations of gas-to-particle partitioning by grouping compounds together within a volatility basis set (13, 24). Within this framework, the volatility bins are separated by one decade in $C^*$ at 300 K, and for

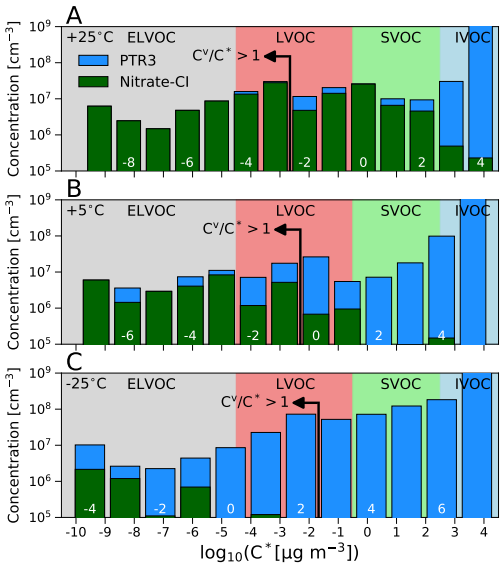


**Fig. 2.** Volatility distributions for representative experiments with similar $\alpha$-pinene ozonolysis rate, (A) +25°C, (B) +5°C and (C) -25°C. The green and blue bars show summed molecular ions observed in the Nitrate-CI and PTR3, respectively. The highest and lowest bin are overflow bins. Volatility bins are defined at 300 K, shifted and widened according to their corresponding temperature. The resulting saturation mass concentration is defined on the x-axis, while $\log_{10} C^*_{300\mathrm{K}}$ is specified by white numbers. Additionally, the bins in supersaturation with $C^v/C^* > 1$ are found left of the indicating arrow.

other temperatures the binned distribution is shifted towards lower saturation mass concentrations. The saturation mass concentration of oxidized organics should follow the Clausius-Clapeyron relation at a constant evaporation enthalpy $\Delta H_{\mathrm{vap}}$, which in turn is linked to $C^*$ at 300 K (13) (see Supporting Information for details).

Fig.2 shows the resulting binned volatility distribution of all observed organic gas-phase compounds for the three representative experiments of Fig.1. Due to the observed comparable growth rates of the three examples, the gas-particle partitioning is expected to be comparable, which is confirmed by the similarity of the observed total volatility distribution over the ELVOC and LVOC ranges. However, it is important that this is only the case due to the additional observed compounds by the PTR3, which, in agreement with Fig.1, mainly detects less oxygenated molecules with $n_O \leq 7$. Earlier work on growth of nucleated particles from $\alpha$-pinene oxidation at +5°C employing only a Nitrate-CI found that the measured HOMs could only explain a fraction of the growth and speculated that the nitrate detection efficiency was progressively lower for less polar (and hence more volatile) species (8). We confirm the missing fraction and find that the PTR3 detects many new compounds not measured by the Nitrate-CI, independent of temperature. At low temperature, fewer polar functional groups are required for a compound to have a low volatility, and thus at +5 °C and even more significantly at -25°C (Panel (B) and (C) respectively) these species observed by the PTR3 contribute substantially in the LVOC and even ELVOC range.

**Particle growth measurements.** We measured growth rates during the experiments with a DMA-train over two different size-intervals, $1.8 - 3.2$ nm and $3.2 - 8$ nm (see Methods for details). Fig.3 shows the measured growth rates versus several gas-phase variables. Panel (A) and (B) show the correlation with the estimated reaction rate of the $\alpha$-pinene ozonolysis during the growth rate measurement. Higher reaction rates, and hence higher product concentrations, lead to higher growth rates, following an exponential relation $m(T, d_p) \cdot [\mathrm{k}(T) \cdot \mathrm{ap} \cdot \mathrm{O_3}]^q$ (see Supplementary Information for details). For a given $\alpha$-pinene ozonolysis reaction rate we find lower growth rates at smaller sizes. The smaller size range also shows a more significant temperature dependency: the growth rates are higher at low temperatures at a given reaction rate. This indicates that the ozonolysis products at the three different temperatures have different properties influencing their ability to condense from molecular cluster sizes onward.

Fig.3 panel (C) and (D) show the measured growth rates versus the total HOM signal observed in the Nitrate-CI only, along with a kinetic curve showing the growth rate if all measured HOMs condensed irreversibly (25). The growth rates of the three different temperatures are clearly separated, but condensation at the kinetic limit for HOMs would give almost identical values. Thus, the total HOM concentration observed in the Nitrate-CI cannot fully describe the observed growth at any temperature. At +25°C several HOMs measured by the Nitrate-CI are classified as SVOC and might not be able to condense, and at -25°C the Nitrate-CI measures only a small fraction of the less oxygenated $\alpha$-pinene oxidation products responsible for particle growth (see Fig.2).

Therefore, panels (E) and (F) of Fig.3 show the growth rates versus a sum, combining both mass spectrometers, over all VBS bins in supersaturation for a given particle size, i.e. with $S = K(D_p) \cdot C^v_{\mathrm{VBS\ bin}} / C^*_{\mathrm{VBS\ bin}} > 1$. A Kelvin-term $K(D_p) = 10^{D_{K10}/D_p}$ accounts for the curvature of the particles, slowing growth of smaller particles. With this simple approach, it is possible to bring the growth measurements at these three different temperatures into reasonable agreement, aligning the data points roughly parallel to the kinetic line. This approach only accounts for bins in supersaturation, which should condense almost kinetically. Especially for the larger size-interval, the measured growth rates are slightly higher than the supersaturated kinetic limits for all temperatures. However, some VBS bins below supersaturation will contribute as well by gas-particle partitioning, which is not considered in this simple approach.

**Comparison with an aerosol growth model.** Aerosol growth is modeled with the same framework as used in (8). However, the model was adopted to take real time measured VBS-distributions from both mass spectrometers as input, without any adjustments of unknown charging efficiencies (see Supporting Information for details).

The most important remaining unknown in the condensation equations is the Kelvin-term and the Kelvin-diameter, describing the curvature effect for the condensation onto the smallest particles:

$$D_{K10} = \log_{10}(e) \cdot \frac{4\sigma M}{RT\rho} \qquad [1]$$

However, the observed size-dependence and especially the growth measurements at diameters $< D_{K10}$ should provide a direct constraint on the curvature effect. For the three representative experiments, we find the best agreement with $D_{K10}(T) = (4.8 \pm 0.8) \cdot (300\,\mathrm{K} \cdot T^{-1})$ nm, which could correspond to a surface tension of $\sigma = 0.03$ N m$^{-1}$, a molecular

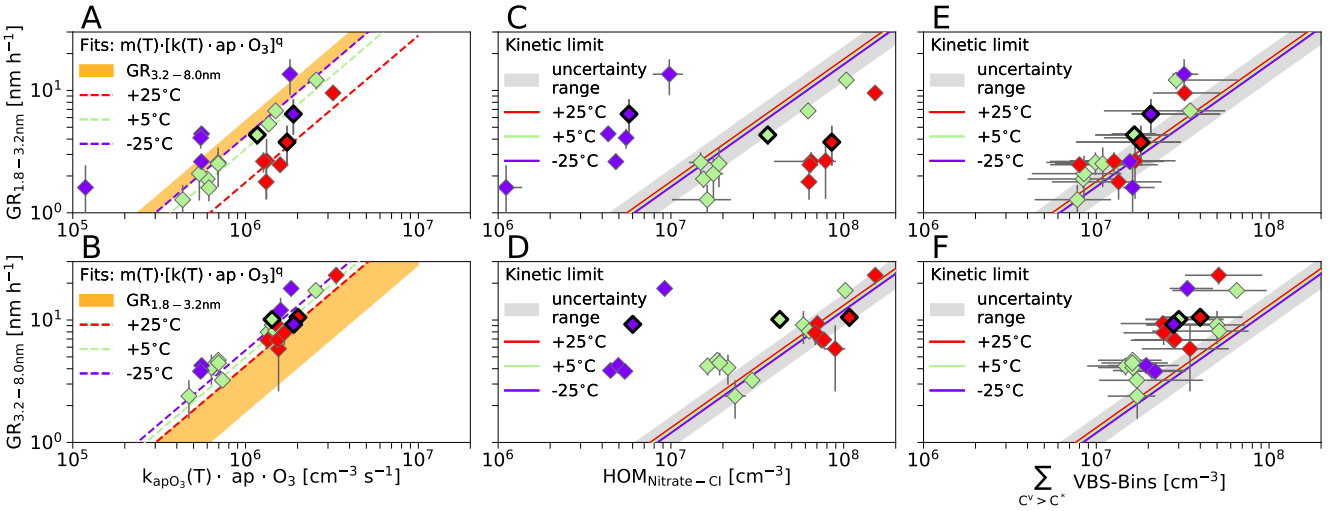


**Fig. 3.** Growth rates measured by the DMA-train in two size intervals (1.8-3.2 nm, panels (A),(C),(E) and 3.2-8 nm, panels (B),(D),(F)) versus several gas phase variables. Representative experiments are highlighted. On the x-axis, panel (A) and (B) show the reacted $\alpha$-pinene rate, panel (C) and (D) show the HOMs observed in the Nitrate-CI and panel (E) and (F) show the amount of condensable material determined by the temperature dependent volatility basis set. Colors in all plots indicate the run temperatures, purple corresponds to -25°C, green to +5°C and red to +25°C. In panel (A) and (B) the light yellow areas shows the range of growth rates of the other size-interval to demonstrate the observed lower growth rates at small diameters. In panels (C)-(F), the gray area illustrates the range of uncertainty on the kinetic condensation limits drawn as solid colored lines. In panel (E) and (F) the error on the sum over the VBS-distribution is determined from the 1 decade uncertainty in the volatility definition.

mass of $M = 320$ g mol$^{-1}$ and a density of $\rho = 1400$ kg m$^{-3}$, values typical for a LVOC HOM. Fig.4 shows the resulting predicted growth rates and their size-dependence in comparison with the measurements. The agreement between modeled and measured growth rate at the smallest sizes is within the uncertainties of the measurements. Other values for $D_{K10}$, e.g. $D_{K10}(300K) = 3.75$ nm, used previously, lead to a significant overestimation of the observed growth rates at the smallest diameters for all temperatures. Another reason for the higher $D_{K10}$ could be an underestimation of the volatility of the most oxygenated compounds (26). Above 5 nm, the model agrees well with the observations at all temperatures. Considering the 1 decade uncertainty in saturation mass concentration (see Supporting Information for details), we achieve reasonable mass balance for growth of freshly nucleated particles between 2 and 30 nm over a wide range of conditions.

Although there is no disagreement of the model with the measurements, within the uncertainties, there are several contributions that we have not considered. First, some condensable compounds might still be undetected by the two used ionization-chemistries. Additionally, fragmentation of molecules within the instruments might disturb the volatility estimate. Second, as well the temperature dependence of organic volatilities is subject to uncertainties (11). Third, we do not model any particle phase reactions, such as oligomerisation. Reactive uptake is thought to be more important at larger particle sizes (27), again in part because of the Kelvin effect (28).

## Conclusion

Organics play a leading role in atmospheric new particle formation and growth and thus govern the global budget of CCN. VOC oxidation products in the atmosphere make up a substantial portion of condensing vapors causing growth of existing particles. Because oxidized organics span a wide range of volatilities, temperature is a crucial parameter. We have shown that the combination of two mass spectrometers, both using different ionization techniques, and consideration of the volatility distribution of the measured compounds, here with a volatility basis set, gives a sufficient constraint of the gas-phase products, to comprehensively describe growth over a wide temperature range. The measurements are in good agreement with an aerosol growth model and for the first time a direct estimate of the Kelvin diameter for organics of 4.8 nm could be inferred.

Temperature influences the growth by organics from dark $\alpha$-pinene ozonolysis in several ways via competing processes. This is illustrated in Fig.5, where the oxidation products containing 4 oxygen atoms are compared to the oxidation products containing 10 oxygen atoms with respect to their average saturation mass concentration and the measured concentration for three experiments with a comparable $\alpha$-pinene ozonolysis reaction rate. While for both groups of compounds the volatility decreases with decreasing temperature, the measured concentrations increase with increasing temperature for the $O_{10}$ monomers at similar $\alpha$-pinene ozonolysis reaction rates. This is due to the temperature dependence of the unimolecular auto-oxidation reactions. It is highly likely that the intramolecular H-atom transfer reactions have significantly higher activation energies than radical-radical termination reactions, and so it is reasonable that the extent of auto-oxidation will increase with increasing temperature (29). As these intramolecular reactions have to occur several times in order to form higher oxygenated molecules, measured concentrations of $O_{10}$ compounds drop significantly as temperature decreases.

Our precision measurement of particle growth rates across the critical size range from 2 - 30 nm reveal that organic condensation drives particle growth at a similar rate over a wide temperature range, when the precursor oxidation rate is held constant. This is due to counterbalancing temperature-dependent effects: lower volatility but also less extensive oxygenation at lower temperature. The competing processes

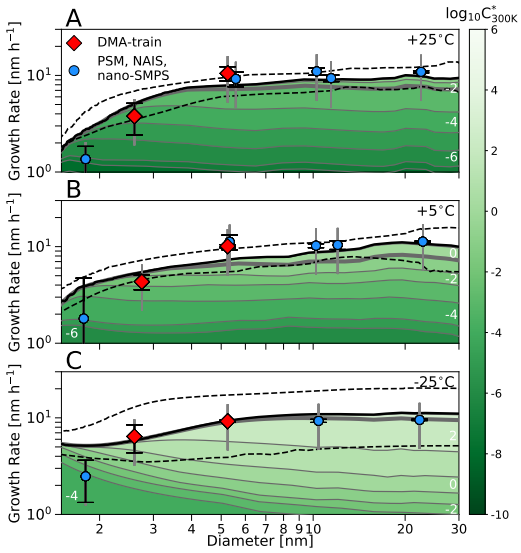


**Fig. 4.** Modeled and measured growth rate versus particle diameter. (A) +25°C at increasing $\alpha$-pinene ozonolysis reaction rates ($\sim$1.7-2.3$\cdot 10^6$cm$^{-3}$s$^{-1}$) (B) +5°C at increasing reaction rates ($\sim$1.2-1.8$\cdot 10^6$cm$^{-3}$s$^{-1}$) (C) -25°C at constant reaction rates ($\sim$1.9$\cdot 10^6$cm$^{-3}$s$^{-1}$). The thick black lines indicates the modeled total growth rate and the dashed black lines indicate the associated uncertainty resulting from a $\pm$one bin shift of the VBS-distribution. The contribution of the different bins of the VBS-distribution is illustrated by the colored areas, where white numbers and the color code represent the saturation mass concentration at 300 K for all three cases. The contribution below the thick gray line is from bins with $C^v > C^*$. For the measured growth rates, red diamonds show the DMA-train (shown as well in Fig.3) and blue circles other instruments (see Supporting Information for details). The capped black errorbar shows the statistical uncertainty of the single measurements, while the gray errorbar gives the 50 % systematic uncertainty of the appearance time method.

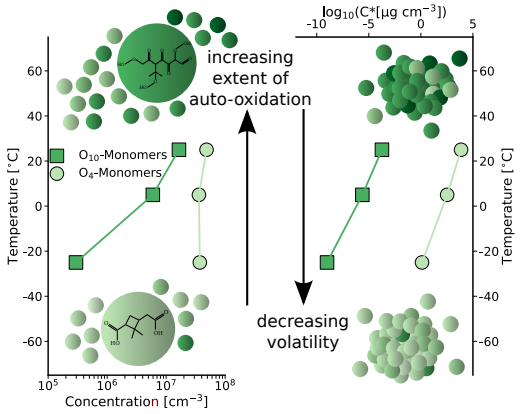


**Fig. 5.** Overview over the competing processes and their temperature dependence. The left panel shows the summed measured concentration of the $O_4$ and $O_{10}$ monomer ($C_{6-10}$) compounds. The right panel shows the averaged saturation mass concentration of the same groups of compounds. Data are taken from three experiments with comparable $\alpha$-pinene ozonolysis reaction rate. The sketch on the left panel illustrates the higher measured concentrations at higher temperatures, especially of highly oxygenated products. The sketch on the right panel shows that growth at cold temperature can proceed already with the condensation of lower oxygenated products due to the decrease in volatility.

described in Fig.5 are thus of the same order of magnitude. This suggests a crucial role for organics in aerosol growth across the wide temperature range of the troposphere. Not only due to higher emission and ozonolysis reaction rates, but also due to rapid auto-oxidation to highly oxygenated states, organics can influence aerosol growth dramatically in warm regions. However, due to the strong drop in volatility of even modestly oxygenated organic products at low temperature, organics can drive aerosol growth also in cold regions, e.g. at high altitudes and the sub-arctic. Global aerosol models therefore need to implement robust descriptions of these processes, not only considering the first order rate constants of ozonolysis and OH reactivity, but rather a more detailed description of organic chemistry and its temperature dependence. Precision measurements with a complementary set of mass spectrometers and particle-size-distribution measurements in the crucial region below 10 nm provide important constraints for model predictions of the contribution of gas-to-particle conversion to the global budget of cloud condensation nuclei.

## Materials and Methods

**The CLOUD chamber.** The CERN CLOUD chamber is a 26.1 m$^3$ electro-polished stainless steel vessel, surrounded by a thermal housing capable of stabilizing temperature in a range from -65 °C to +100 °C with $\pm$0.1 K precision (30). The chamber is equipped with a gas control system achieving extremely high purities by mixing boil-off nitrogen and boil-off oxygen at the atmospheric ratio of 79:21. Highly pure trace gases can be precisely added at the ppt level. Before the start of the experiments the chamber was heated to 100 °C and rinsed with ultra-pure water for cleaning. This assured operation at contaminant levels of less than $5 \cdot 10^4$ cm$^{-3}$ $H_2SO_4$ and total organics below 150 pptv (15, 20).

A high-voltage field of $\pm$30 kV can be applied between two electrode grids, located at the top and bottom of the chamber. The electric field sweeps out all ions from the chamber allowing for ion-free experiments. If the field is switched off, ions are created by the impact of galactic cosmic rays and decay products from ambient radioactivity.

Experiments were conducted as follows: At 38 % relative humidity, with no $SO_2$ and no $NO_x$ present in the chamber, stable ozone concentrations of 30-40 ppb were established. Under dark conditions, i.e.without any additional OH radical production mechanism except from the ozonolysis itself, the high-voltage field was switched on, to perform experiments under neutral conditions first. Injection of $\alpha$-pinene initiated the ozonolysis reaction and the subsequent formation of particles. After steady-state $\alpha$-pinene concentrations were reached and particle growth was measured up to at least 10 nm, the high-voltage field is switched off. Ions now present in the chamber lead to a significant increase in nucleation rate (7). Therefore two growth rate measurements can eventually be performed as the size-distribution will show two growing particle populations. Moreover, the second measurement is almost independent of changing gas concentrations as the steady-state is already reached during the neutral experiments. As no significant effect on growth due to the different ionization conditions was found all measurements are treated equally in this study.

**Measurement of particle growth.** Apparent particle growth rates are inferred from particle-size-distribution measurements with the appearance time method (10), as it was done in previous comparable studies (8, 14). Particle-size-distributions are measured by several sizing instruments optimized for a certain size range. Each instrument was thereby treated separately but we found comparable results in the overlapping regions for all presented experiments (See Supporting Information for details).

Key part of this study is the precision measurement of particle-size-distributions in the size range between 1.8-8 nm by a newly developed instrument, a DMA-train (23). It uses six differential mobility analyzers in parallel with the classified size fixed for every device. Subsequent detection of the size-selected aerosol is done by the usage of six condensation particle counters. As no scanning is involved, high counting statistics at a single size is achieved, providing unprecedented high sensitivity to low number concentrations in the crucial sub 10-nm range.

**Gas-phase measurements.** Gas phase compounds were measured by high-resolution mass spectrometry. For this study two different instruments with two different chemical ionisation techniques were combined in order to obtain a more detailed overview of the neutral gas phase species present during the $\alpha$-pinene ozonolysis experiments.

Using an atmospheric-pressure-interface, the rather selective ionization technique of a chemical-ionisation mass spectrometer using nitrate ($HNO_3$)($NO_3^-$) as the reagent ion (21) was used to obtain a very clean spectrum of HOMs (6). The broad ionization efficiency of $H_3O^+$-water clusters was deployed in a novel proton-transfer-reaction time-of-flight mass spectrometer to ionize VOCs as well as semi-volatile organic compounds (SVOCs) and HOMs (22). While the Nitrate-CI is calibrated to the response of $H_2SO_4$, the response of the PTR3 to HOMs is assumed to behave comparably to Butanon (22). Inlet loss corrections for HOMs have to be applied to both instruments and are adjusted for the PTR3 to give good overlap for peaks observed in both instruments (see Supporting Information for details).

When combining the two mass spectrometers, for molecular ion signals observed in both instruments the higher signal is used. Both spectra are background subtracted and therefore a weaker signal in either of the mass spectrometers could point towards a lower ionisation efficiency.

**ACKNOWLEDGMENTS.** We thank T.Kurten and N.Hyttinen for providing helpful COSMOtherm volatility estimates. We thank the European Organization for Nuclear Research (CERN) for supporting CLOUD with important technical and financial resources and for providing a particle beam from the CERN Proton Synchrotron. This research has received funding from the EC Seventh Framework Programme (Marie Curie Initial Training Networks 'CLOUD-TRAIN' (no. 316662), German Federal Ministry of Education and Research (no. 01LK1222A, no. 01LK1601A), the Swiss National Science Foundation (projects no. 20FI20_159851, 200020_172602, 20FI20_172622), the Austrian Research Funding Association FFG (Project Number 846050), ERC-Consolidator Grant NANODYNAMITE 616075, ERC-Advanced Grant DAMOCLES 692891, ERC-Starting Grant COALA 638703, Horizon 2020 Marie Sklodowska-Curie Grant 656994 ("Nano-CAVa"), the Presidium of the Russian Academy of Sciences, the Program "High energy physics and neutrino astrophysics" 2015. We also thank K.Ivanova, P. Carrie, L.-P. De Menezes, J. Dumollard, F. Josa, I. Krasin, R. Kristic, A. Laassiri, O. S. Maksumov, B. Marichy, H. Martinati, S. V. Mizin, R. Sitals, A. Wasem and M. Wilhelmsson for their contributions to the experiment.

1. Gordon H, et al. (2017) Causes and importance of new particle formation in the present-day and preindustrial atmospheres. *J. Geophys. Res.-Atmos.* 122. 2017JD026844.
2. Lehtinen KE, Maso MD, Kulmala M, Kerminen VM (2007) Estimating nucleation rates from apparent particle formation rates and vice versa: Revised formulation of the kerminen–kulmala equation. *J. Aerosol Sci.* 38(9):988 – 994.
3. Pierce JR, Adams PJ (2007) Efficiency of cloud condensation nuclei formation from ultrafine particles. *Atmos. Chem. Phys.* 7(5):1367–1379.
4. Riipinen I, et al. (2012) The contribution of organics to atmospheric nanoparticle growth. *Nat. Geosci.* 5:453–458.
5. Guenther AB, et al. (2012) The model of emissions of gases and aerosols from nature version 2.1 (megan2.1): an extended and updated framework for modeling biogenic emissions. *Geosci. Model Dev.* 5(6):1471–1492.
6. Ehn M, et al. (2014) A large source of low-volatility secondary organic aerosol. *Nature* 506:476–479.
7. Kirkby J, et al. (2016) Ion-induced nucleation of pure biogenic particles. *Nature* 533:521–526.
8. Tröstl J, et al. (2016) The role of low-volatility organic compounds in initial particle growth in the atmosphere. *Nature* 533:527–531.
9. Gordon H, et al. (2016) Reduced anthropogenic aerosol radiative forcing caused by biogenic new particle formation. *P. Nat. Acad. Sci. USA* 113(43):12053–12058.
10. Kulmala M, et al. (2013) Direct observations of atmospheric aerosol nucleation. *Science* 339(6122):943–946.
11. Donahue NM, Trump ER, Pierce JR, Riipinen I (2011) Theoretical constraints on pure vapor-pressure driven condensation of organics to ultrafine particles. *Geophys. Res. Lett.* 38(16):n/a–n/a. L16801.
12. Kulmala M, Kerminen VM, Anttila T, Laaksonen A, O'Dowd CD (2004) Organic aerosol formation via sulphate cluster activation. *J. Geophys. Res.-Atmos.* 109(D4). D04205.
13. Donahue NM, Epstein SA, Pandis SN, Robinson AL (2011) A two-dimensional volatility basis set: 1. organic-aerosol mixing thermodynamics. *Atmos. Chem. Phys.* 11(7):3303–3318.
14. Lehtipalo K, et al. (2016) The effect of acid–base clustering and ions on the growth of atmospheric nano-particles. *Nat. Commun.* 7:11594.
15. Frege C, et al. (2018) Influence of temperature on the molecular composition of ions and charged clusters during pure biogenic nucleation. *Atmos. Chem. Phys.* 18(1):65–79.
16. Bianchi F, et al. (2016) New particle formation in the free troposphere: A question of chemistry and timing. *Science* 352(6289):1109–1112.
17. Murphy BN, Julin J, Riipinen I, Ekman AML (2015) Organic aerosol processing in tropical deep convective clouds: Development of a new model (CRM-ORG) and implications for sources of particle number. *J. Geophys. Res.-Atmos.* 120(19):10,441–10,464. 2015JD023551.
18. Wang J, et al. (2016) Amazon boundary layer aerosol concentration sustained by vertical transport during rainfall. *Nature* 539:416–419.
19. Andreae MO, et al. (2018) Aerosol characteristics and particle production in the upper troposphere over the amazon basin. *Atmos. Chem. Phys.* 18(2):921–961.
20. Kirkby J, et al. (2011) Role of sulphuric acid, ammonia and galactic cosmic rays in atmospheric aerosol nucleation. *Nature* 476:429–433.
21. Jokinen T, et al. (2012) Atmospheric sulphuric acid and neutral cluster measurements using CI-APi-TOF. *Atmos. Chem. Phys.* 12(9):4117–4125.
22. Breitenlechner M, et al. (2017) Ptr3: An instrument for studying the lifecycle of reactive organic carbon in the atmosphere. *Anal. Chem.* 89(11):5824–5831. PMID: 28436218.
23. Stolzenburg D, Steiner G, Winkler PM (2017) A DMA-train for precision measurement of sub-10 nm aerosol dynamics. *Atmos. Meas. Tech.* 10(4):1639–1651.
24. Donahue NM, Robinson AL, Stanier CO, Pandis SN (2006) Coupled partitioning, dilution, and chemical aging of semivolatile organics. *Environ. Sci. Technol.* 40(8):2635–2643.
25. Nieminen T, Lehtinen KEJ, Kulmala M (2010) Sub-10 nm particle growth by vapor condensation – effects of vapor molecule size and particle thermal speed. *Atmos. Chem. Phys.* 10(20):9773–9779.
26. Kurtén T, et al. (2016) Alpha-pinene autoxidation products may not have extremely low saturation vapor pressures despite high O:C ratios. *J. Phys. Chem. A* 120(16):2569–2582. PMID: 27049168.
27. Apsokardu MJ, Johnston MV (2018) Nanoparticle growth by particle-phase chemistry. *Atmos. Chem. Phys.* 18(3):1895–1907.
28. Chuang WK, Donahue NM (2017) Dynamic consideration of smog chamber experiments. *Atmos. Chem. Phys.* 17(16):10019–10036.
29. Praske E, et al. (2018) Atmospheric autoxidation is increasingly important in urban and suburban north america. *P. Nat. Acad. Sci. USA* 115(1):64–69.
30. Dias A, et al. (2017) Temperature uniformity in the CERN CLOUD chamber. *Atmos. Meas. Tech.* 10(12):5075–5088.

## Supporting Information (SI)

**Appearance time method for growth rate determination.** Particle growth rate measurements were performed with the appearance time method, which can be used especially in chamber experiments, where a clear front of a growing particle population can be identified during most nucleation experiments.

The particle-size distribution was measured by a comprehensive set of four different instruments. Below 2.5 nm, a particle size magnifier in scanning mode was used (31). The size range between 1.8-8 nm was covered by a DMA-train (23). Above 8 nm a scanning mobility particle sizer system, TSI nano-SMPS model 3982, measured up to 65 nm (32). Additionally, a neutral cluster and air ion spectrometer (NAIS) measured between 3-42 nm (33).

Considering the evolution of particle size-distribution binned into different size-channels, the signal in each size-channel is fitted individually with a four parameter sigmoid function using a least-square algorithm:

$$S_{\mathrm{d_p}}(t) = \frac{a-b}{1+(t/t_{\mathrm{app}})^d} + b, \qquad [S1]$$

where $a$ and $b$ represent the background and plateau value of the sigmoid function respectively, $d$ is a parameter for the steepness of the rising signal and $t_{\mathrm{app}}$ is the time at which the 50 % value between plateau and background is reached.

A representative fit for a 3.2 nm size channel of the DMA-train is shown in Fig. S1 (A). All size-channels are cross-checked manually after the automated fitting and a statistical error of $t_{\mathrm{app}}$ is estimated from the covariance of the fit-result. The values obtained for $t_{\mathrm{app}}$ can be plotted against the corresponding diameter as shown in Fig.S1 (B). A linear fit with an orthogonal distance regression is used to take into account both the uncertainties of $t_{\mathrm{app}}$ and of the diameter of the size-channels. The resulting value of the slope and its associated error can be interpreted as an apparent particle growth rate and its statistical uncertainty. However, this growth rate does not necessarily represent the growth caused by pure condensation, as it omits coagulation and, in chamber experiments, wall losses, which both alter the particle size-distribution (34). Therefore, a systematic uncertainty of the method is estimated to be 50 % (35).

For the DMA-train two size-intervals for the growth rate measurement were defined: One between 1.8-3.2 nm and one between 3.2-8 nm. The choice of the size-intervals is arbitrary but proofed to be representative to show differences between early and later growth. In (8) it was shown that growth driven by biogenic organics shows only a minor size-dependence above 5 nm, i.e. the upper growth rate size-interval of the DMA-train is representative for growth >5 nm.

**Absolute HOM concentration measurements using Nitrate–CI-APi-ToF.** The Nitrate-CI-APi-ToF (Nitrate-CI) uses negative nitrate, $(HNO_3)(NO_3^-)$, as reagent ion (36), which shows high charging efficiencies towards $H_2SO_4$ and HOMs. The concentration of a HOM species is estimated via

$$[\mathrm{HOM}_i] = C \cdot T_i \cdot \mathrm{SL}_{\mathrm{HOM}_i} \cdot \ln\left(1 + \frac{[\mathrm{HOM}_i \cdot \mathrm{NO}_3^-]}{\sum_{j=0}^{2}[\mathrm{NO}_3^- \cdot (\mathrm{HNO}_3)_j]}\right) \qquad [S2]$$

Here $[\mathrm{HOM}_i \cdot \mathrm{NO}_3^-]$ is the background corrected peak area which is normalized to the intensity of the main reagent ions. To obtain a quantitative concentration, three factors are applied: First, a calibration factor $C$, which is inferred from a calibration using sulfuric acid (37) and assuming that all detected HOMs have the same ionization efficiency (6). Second, a mass dependent transmission efficiency $T_i$ of the APi-ToF can be inferred in a seperate experiment by depleting the reagent ions with several perfluorinated acids (38). Third, sampling line losses $\mathrm{SL}_{\mathrm{HOM}_i}$ are estimated assuming laminar flow diffusional losses in the sampling lines (39) with a diffusion coefficient of HOMs scaling with the molecular mass $M_i$ of the compound via $D[\mathrm{cm^2 s^{-1}}] = 0.31 \cdot M_i^{-1/3}$ at 278 K, determined from wall loss measurements in the CLOUD chamber. As the sampling lines of the Nitrate-CI are thermally insulated, for other experiment temperatures $D \propto (T/278K)^{1.75}$ is assumed. As the compounds detected by the Nitrate-CI are mostly classified ELVOC or LVOC in the temperature range of this study, we can assume that they all get lost irreversibly to sampling line walls due to diffusion.

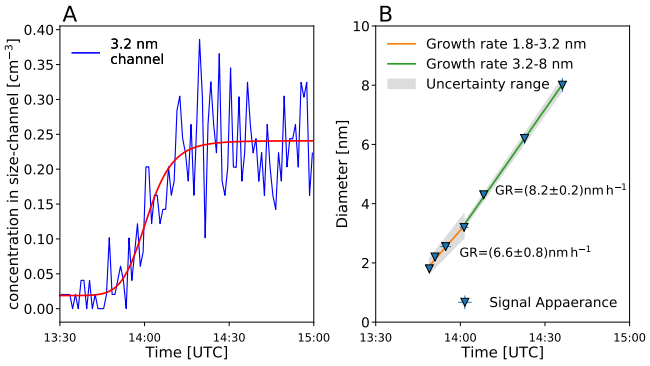


**Fig. S1.** Example for a representative determination of the particle growth rate with the appearance time method for data obtained by the DMA-train. Panel (A) shows the sigmoid function fit to the measured concentration within the 3.2 nm channel. Panel (B) shows the orthogonal distance regression for the growth rate determination in two intervals.

**Absolute concentration measurements of oxidized organics using PTR3-ToF.** The PTR3-ToF (PTR3) uses $(H_3O^+)(H_2O)_n$ clusters as reagent ions, ionizing $\alpha$-pinene as well as first and higher order oxidation products by proton transfer or ligand switch reactions (22). A contact minimized laminar flow inlet system with core sampling is used to transfer the sample air into the tripole reaction chamber operated at 80 mbar and reduces transmission losses. The $(H_3O^+)(H_2O)_n$ cluster ion distribution can be regulated by a radio-frequency-amplitude applied to the tripole rods without influencing the reaction time. Increased pressure in the reaction region and longer reaction times compared to traditional PTR instruments yield a 500 fold increased sensitivity to a broad range of organics. At the operating conditions of the PTR3, secondary reactions of ionized species with the most abundant neutral VOCs in the sample gas are limited to less then one percent at the highest measurable concentrations. The new instrument bridges the gap between precursor measurements at ppbv level to HOM measurements at sub ppt level, complementing atmospheric pressure CIMS techniques.

A quadrupole interfaced Long-ToF mass spectrometer (TOFWERK AG, Thun, Switzerland) is providing the high mass resolving power needed to separate isobaric compounds. We obtained more than 1500 individual mass peaks, excluding isotopes, during $\alpha$-pinene ozonolysis experiments. A multi-peak fitting algorithm is applied to separate the major compounds and assign chemical sum formulas. Extracting the relevant signals is done omitting all masses rising less than $3\sigma$ above chemical background noise during ozonolysis measurements and removing peaks with possible uncertainties caused by interference of higher neighboring peaks. $(H_3O^+)(H_2O)_n$ clusters are known to be soft ionization reagent ions. Nevertheless we cannot exclude completely fragmentation of some ionized HOMs loosing most likely $H_2O$ especially when containing an (-OOH) group.

The PTR3 was calibrated with a gas standard containing 1 ppm of 3-hexanone, heptanone and $\alpha$-pinene in nitrogen, which was dynamically diluted by a factor of 1000 in VOC-free air to contain 1 ppbv of each compound. Duty cycle corrected counts per second *dcps* are used in order to compensate for the mass-dependent transmission of the TOF mass spectrometer ($dcps(i) = cps(i) \cdot (101/m_i)^{1/2}$) (22). For 3-hexanone and heptanone we obtained a sensitivity which is in agreement with the calculated sensitivity taking into account the duty cycle corrected $(H_3O^+)(H_2O)_n$ regent ion count rates, the pressure and the reaction time in the reaction chamber (80 mbar; 3 ms) and using $2-3 \cdot 10^{-9}\mathrm{cm^3 s^{-1}}$ as a fast reaction rate constant close to the collisional limit value. Consequently, only lower end product concentrations can be given.

In a previous $\alpha$-pinene ozonolysis study PTR3 results showed quantitative agreement for several HOMs with the Nitrate-CI (22). The authors estimated 80 % inlet losses for low-volatile molecules

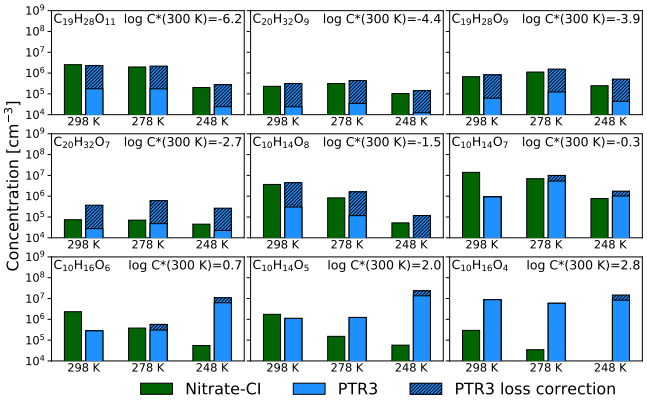


**Fig. S2.** Quantitative comparison of selected peaks observed in both mass spectrometers and its temperature dependence for three representative runs with similar $\alpha$-pinene ozonolysis rate. The correction for PTR3 compounds to account for sampling line losses and the additional 80 % wall loss inside the PTR3 ion source are displayed by the hatched area.

with $n_O \geq 5$, bringing the two instruments into reasonable quantitative agreement for common molecular ion signals. However, the assumption for the Nitrate-CI, that all detected molecules get lost on contact with sampling line walls, does not hold for all substances measured by the PTR3. In the transition from SVOC to LVOC the partitioning of substances between inlet line walls and sample gas is temperature dependent. We therefore extended the approach of (22) with our knowledge about an approximate volatility of the measured compounds. Assuming that all molecules in the LVOC and ELVOC range get lost by diffusion (the diffusion coefficient of a molecule is estimated similar to the Nitrate-CI) according to (39), we can apply a temperature dependent loss-correction for the sampling line losses, which is split up into three sections:

$$\eta_{\mathrm{tot}} = \eta_{\mathrm{line,int}}(T) \cdot \eta_{\mathrm{line,ext}}(298\mathrm{K}) \cdot \eta_{\mathrm{PTR3}}(310\mathrm{K}) \quad [S3]$$

We account for losses at the sampling line within the CLOUD chamber $\eta_{\mathrm{line,int}}$ at chamber temperature $T$, as well as losses occurring at the sampling line outside the chamber at room temperature $\eta_{\mathrm{line,ext}}$ (as it was not thermally insulated) and losses within the PTR3 instrument heated to 37°C $\eta_{\mathrm{PTR3}}$. Therefore, for each sampling section other molecules might be subject to losses according to their temperature-dependent volatility classification.

**Comparison of the used mass spectrometers.** The considerations of the two previous sections result in the comparison for data obtained in three representative experiments at three different temperatures which is shown in Fig.S2, where $\eta_{\mathrm{line,int}}$ and $\eta_{\mathrm{line,ext}}$ are calculated assuming diffusional losses similar to the Nitrate-CI and $\eta_{\mathrm{PTR3}}$ is estimated to correct for the 80% discrepancy found in (22). For higher oxygenated molecules the agreement between both mass spectrometers is in a reasonable range including the additional loss term $\eta_{\mathrm{PTR3}}$ for losses within the PTR3 ion source and inlet. This indicates that the loss in measured concentration from +25°C to -25°C for the three experiments at similar initial precursor oxidation rates is caused by the reduced reaction rates of the auto-oxidation process. For lower temperatures and lower oxidized states ($n_O$ = 4/5/6) a discrepancy between the instruments gets significant. However, even at elevated temperatures, the Nitrate-CI is only detecting a small fraction of all oxidation products with $n_O = 5/6$ observed by the PTR3. Therefore it is concluded that the increasing discrepancy is likely due to a lowered sensitivity of the Nitrate-CI for such compounds. The ionization efficiency in the Nitrate-CI depends on the relative binding energy of a $(HNO_3)(NO_3^-)$ cluster compared to a $(Analyte)(NO_3^-)$ cluster (40). A relative shift in binding energies at lower temperatures that favors $(HNO_3)(NO_3^-)$ clustering instead of $(Analyte)(NO_3^-)$ clustering, could explain the observed decrease of signal for the lower oxidation states for the Nitrate-CI. The higher oxidation states however are unaffected because the $(HOM)(NO_3^-)$ clustering is generally very strong and will always dominate the $(HNO_3)(NO_3^-)$ clustering, which explains the good agreement of the two instruments for higher oxidized states.

**Growth rate parametrization.** Growth rates were parametrized in Fig.3 (A) and (B) by the simple exponential relation $\mathrm{GR}=m(T,d_p)\cdot[\mathrm{k}(T)\cdot\mathrm{ap}\cdot\mathrm{O_3}]^q$, to express the correlation between growth rate and $\alpha$-pinene ozonolysis reaction rate. While the coeffcients $m(T,d_p)$ depend on temperature and size-range of the growth rate measurement, $q$ is chosen to be independent of both. A minimum least-square regression yields the results presented in TableS1.

| Size-Range | m(+25°C) | m(+5°C) | m(-25°C) | q |
|---|---|---|---|---|
| 1.8-3.2 nm | $1.12{\cdot}10^{-7}$ | $2.09{\cdot}10^{-7}$ | $2.67{\cdot}10^{-7}$ | 1.21 |
| 3.2-8.0 nm | $2.66{\cdot}10^{-7}$ | $3.12{\cdot}10^{-7}$ | $3.57{\cdot}10^{-7}$ | 1.21 |

**Table S1.** Resulting parameters from least-square regression for the growth rate parametrization of Fig.3 (A) and (B) by the simple exponential relation $GR = m(T,d_p)\cdot[\mathrm{k}(T)\cdot\mathrm{ap}\cdot\mathrm{O_3}]^q$.

**Volatility of HOMs.** Direct measurements of volatilities of individual HOM are extremely challenging as they are difficult to synthesize and the vapour pressures are too low for current volatility measurement techniques. To overcome this problem, vapour pressures can be inferred by several model calculations, like so-called group contribution methods (41) or parametrizations according to the oxidation state (13). In this study a combined approach is applied.

We use a volatility parametrization according to the carbon $n_C^i$ and oxygen $n_O^i$ number of the specific molecule $i$. This is based on two general observed trends that increasing carbon and increasing oxygen number lower the volatility of oxidized organic molecules. Thus, these quantities are linked to volatility, expressed as the logarithm of the saturation mass concentration $\log_{10} C_i^*$ for compound $i$:

$$\log_{10} C_i^*(300K) = \left(n_C^0 - n_C^i\right)\cdot b_C - n_O^i\cdot(b_O - b_{\mathrm{add}}) - 2\frac{n_C^i n_O^i}{n_C^i + n_O^i} b_{CO} \quad [S4]$$

where the parameter $n_C^0$=25 is the baseline carbon backbone for a volatility of 1 $\mu$g m$^{-3}$ without the addition of any functional groups. $b_C$=0.475 is the roughly half decade decrease in volatility per carbon atom and $b_O$=2.3 is the more than two decade decrease in volatility per oxygen atom assuming an average of (=O) and (-OH) groups. $b_{CO}$ is a non-linearity term. More details can be found in (13).

However, other functionalities e.g. hydroperoxides (-OOH) and covalently bound dimers are not included in $b_O$, but are both abundant in HOMs from $\alpha$-pinene ozonolysis. To account for these specific attributes, a representative set of proposed products (8, 26) with known structure is analyzed with the group contribution method SIMPOL (41). The results are fitted with Eq. S4 including a free parameter $b_{\mathrm{add}}$ altering the effect of oxygen $b_O$. Monomer and dimer products are fitted separately allowing this parameter to include the covalent binding. The resulting parametrisation at 300 K is shown in Fig. S3. The free parameter yields $b_{\mathrm{add}} = 0.90$ for monomers and $b_{\mathrm{add}} = 1.13$ for dimers. Accordingly, for any $\alpha$-pinene ozonolysis product with unambiguously identified composition, a volatility can be calculated.

However, computed volatilities from group-contribution methods generally tend to underestimate vapour pressures at low vapour pressures. A recent study investigating the volatility of $\alpha$-pinene oxidation products with quantum-chemical based model calculations found large deviations due to intramolecular H-bonds (26). These deviations were significant especially for highly oxygenated monomers and dimers, while the agreement for the higher volatilities was much better.

This study focuses on the temperature dependence of the volatilities which is described by:

$$\log_{10} C^*(T) = \log_{10} C^*(300K) + \frac{\Delta H_{\mathrm{vap}}}{R\,\ln(10)}\left(\frac{1}{300} - \frac{1}{T}\right) \quad [S5]$$

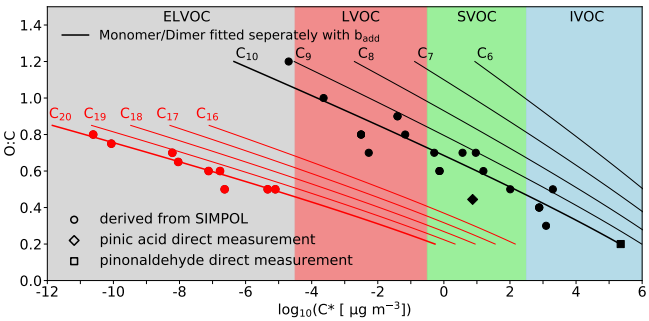


**Fig. S3.** Volatility model used in this study. For a representative set of proposed products from $\alpha$-pinene ozonolysis the known structure is used to calculate the volatility by the group-contribution method SIMPOL or are directly measured by (42, 43). Results are fitted with the proposed relationship from (13) including a free parameter for the oxygen dependence.

The evaporation enthalpy $\Delta H_{\mathrm{vap}}$ can be linked to the saturation mass concentration at 300 K $\log_{10} C^*(300K)$ according to (13) and combined with (44):

$$\Delta H_{\mathrm{vap}} \left[\mathrm{kJ\,mol^{-1}}\right] = -5.7 \cdot \log_{10} C^*(300K) + 129 \qquad [S6]$$

The correlation between volatility at 300 K and the evaporation enthalpy $\Delta H_{\mathrm{vap}}$ is very comparable for approaches like (44), (13) and (26). Moreover, the shift in volatility due to temperature in this study is most important for oxygenated compounds with volatilities around $\log_{10} C^*(300K) \approx 0$, at the transition between LVOC and SVOC. For those molecules also the predictions of the volatility between the different methods don't differ drastically (26). Therefore, we assume an overall uncertainty of the volatility description of $\pm 1$ bin (i.e. 1 decade in $C^*(300K)$ for volatility distributions within a volatility basis set). This uncertainty is shown Fig.3 panel (E) and (F) and gives the method uncertainties in Fig.4.

**Aerosol growth model.** The measured VBS-distributions can be used to model aerosol growth. The modeling framework is based on the one used in (8) but simplified for the input of direct VBS-distribution measurements. Starting from a VBS-distribution at $t = 0$ the growth of a monodisperse population of nucleated particles at an initial size of 1.2 nm mobility diameter is modeled. Every VBS bin is treated like a single surrogate molecule having the properties of the averaged mass and concentration of the bin. It is assumed that the measured gas-phase concentrations are in steady-state with losses to particles and chamber walls. The condensation flux $\phi_{i,p}$ of every VBS bin $i$ should then follow:

$$\phi_{i,p} = N_p \cdot \sigma_{i,p}, \cdot k_{i,p} \cdot F_{i,p} \qquad [S7]$$

$N_p$ gives the number concentration of particles of a given size. $\sigma_{i,p} = \pi/4(d_p + d_i)^2$ is the particle-vapor collision cross-section including the diameter of the monodisperse particle population $d_p$ and mass-diameter of the VBS bin $d_i$. $k_{i,p} = \alpha_{i,p}\nu_{i,p}\beta_{i,p}$ is the deposition rate of vapor molecules at surface, with $\alpha_{i,p}$ the mass accommodation coefficient, $\nu_{i,p} = (8RT/(\pi\mu_{i,p}))^{1/2}$ the center of mass velocity for particle and vapor (with the reduced mass $\mu_{i,p} = (M_i M_p)/(M_i + M_p)$) and $\beta_{i,p}$ the correction factor for non-continuum dynamics (45). $F_{i,p}$ is the driving force of condensation, closely related to the saturation ratio $S_i$ of the VBS bin by $F_{i,p} = C_i^0(S_i - X_{i,p}\gamma_{i,p}K_{i,p})$. This driving force of condensation for a VBS bin $i$ gives the difference between gas phase activity $S_i$ and particle phase activity $(X_{i,p}\gamma_{i,p}K_{i,p})$, which includes the Raoult term $X_{i,p}\gamma_{i,p}$ to account for the mixture effect of the particles and the Kelvin-term $K_{i,p} = \exp(4\sigma M/(RT\rho d_p))$ accounting for the curvature effect of the particle surface. The model assumes an ideal mass based solution, i.e. the condensed phase activity is the mass fraction $X_{i,p}$ and hence $\gamma_{i,p} = 1$. Therefore we use $C*$ as saturation mass concentration throughout this study, as $C^* = \gamma_{i,p}C^0$.

Solving the above condensation equations for the measured evolution of the VBS-distribution assuming this distribution always reflects a steady-state between production from $\alpha$-pinene ozonolysis and wall losses and following the growing monodisperse aerosol population, yields a diameter versus time evolution which can be connected to a growth rate.

Besides from the different input VBS-distributions at different temperature, only the Kelvin-term and the collision-frequency include a temperature dependence.


31. Vanhanen J, et al. (2011) Particle size magnifier for nano-cn detection. *Aerosol Sci. Tech.* 45(4):533–542.
32. Tröstl J, et al. (2015) Fast and precise measurement in the sub-20 nm size range using a scanning mobility particle sizer. *J. Aerosol Sci.* 87:75–87.
33. Manninen HE, et al. (2009) Long-term field measurements of charged and neutral clusters using neutral cluster and air ion spectrometer (nais). *Boreal Environ. Res* 14:591–605.
34. Pichelstorfer L, et al. (2018) Resolving nanoparticle growth mechanisms from size- and time-dependent growth rate analysis. *Atmos. Chem. Phys.* 18(2):1307–1323.
35. Lehtipalo K, et al. (2014) Methods for determining particle size distribution and growth rates between 1 and 3 nm using the particle size magnifier. *Boreal Environ. Res.* 19(suppl. B):215–236.
36. Kürten A, Rondo L, Ehrhart S, Curtius J (2011) Performance of a corona ion source for measurement of sulfuric acid by chemical ionization mass spectrometry. *Atmos. Meas. Tech.* 4(3):437–443.
37. Kürten A, Rondo L, Ehrhart S, Curtius J (2012) Calibration of a chemical ionization mass spectrometer for the measurement of gaseous sulfuric acid. *J. Phys. Chem. A* 116(24):6375–6386. PMID: 22364556.
38. Heinritzi M, et al. (2016) Characterization of the mass-dependent transmission efficiency of a cims. *Atmos. Meas. Tech.* 9(4):1449–1460.
39. Gormley PG, Kennedy M (1948) Diffusion from a stream flowing through a cylindrical tube. *P. Roy. Irish Acad. A* 52:163–169.
40. Hyttinen N, Rissanen MP, Kurtén T (2017) Computational comparison of acetate and nitrate chemical ionization of highly oxidized cyclohexene ozonolysis intermediates and products. *J. Phys. Chem. A* 121(10):2172–2179. PMID: 28234483.
41. Pankow J, Asher W (2008) SIMPOL.1: a simple group contribution method for predicting vapor pressures and enthalpies of vaporization of multifunctional organic compounds. *Atmos. Chem. Phys.* 8:2773–2796.
42. Hallquist M, Wängberg I, Ljungström E (1997) Atmospheric fate of carbonyl oxidation products originating from alpha-pinene and delta-3-carene: Determination of rate of reaction with OH and NO3 radicals, UV absorption cross sections, and vapor pressures. *Environ. Sci. Technol.* 31(11):3166–3172.
43. Bilde M, Pandis SN (2001) Evaporation rates and vapor pressures of individual aerosol species formed in the atmospheric oxidation of alpha- and beta-pinene. *Environ. Sci. Technol.* 35(16):3344–3349. PMID: 11529575.
44. Epstein SA, Riipinen I, Donahue NM (2010) A semiempirical correlation between enthalpy of vaporization and saturation concentration for organic aerosol. *Environ. Sci. Technol.* 44(2):743–748. PMID: 20025284.
45. Fuchs N, Sutugin A (1965) Coagulation rate of highly dispersed aerosols. *J. Colloid Sci.* 20(6):492 – 500.